

## PUBLISHED VERSION

Shuo Li, Dongbi Bai, Marco Capelli, Qiang Sun, Shahraam Afshar V., David A. Simpson, Scott Foster, Heike Ebendorff-Heidepriem, Brant C. Gibson, And Andrew D. Greentree  
**Preferential coupling of diamond NV centres in step-index fibres**  
Optics Express, 2021; 29(10):14425-14437

DOI: <http://dx.doi.org/10.1364/OE.417825>

© 2021 Optical Society of America under the terms of the OSA Open Access Publishing Agreement. An OSA-formatted open access journal article PDF may be governed by the OSA Open Access Publishing Agreement signed by the author and any applicable copyright laws. Authors and readers may use, reuse, and build upon the article, or use it for text or data mining without asking prior permission from the publisher or the Author(s), as long as the purpose is non-commercial and appropriate attribution is maintained.

### PERMISSIONS

[https://opg.optica.org/submit/review/copyright\\_permissions.cfm#posting](https://opg.optica.org/submit/review/copyright_permissions.cfm#posting)

#### Author and End-User Reuse Policy

Our policies afford authors, their employers, and third parties the right to reuse the author's Accepted Manuscript (AM) or the final publisher Version of Record (VoR) of the article as outlined below:

Reuse purpose	Article version that can be used under:		
	Copyright Transfer	Open Access Publishing Agreement	CC BY License
Posting by authors on an open institutional repository or funder repository	AM after 12 month embargo	VoR	VoR

#### Attribution

##### Open access articles

If an author or third party chooses to post an open access article published under our OAPA on his or her own website, in a repository, on the arXiv site, or anywhere else, the following message should be displayed at some prominent place near the article and include a working hyperlink to the online abstract in the journal:

© XXXX [year] Optica Publishing Group. Users may use, reuse, and build upon the article, or use the article for text or data mining, so long as such uses are for non-commercial purposes and appropriate attribution is maintained. All other rights are reserved.










When adapting or otherwise creating a derivative version of an article published under our OAPA, users must maintain attribution to the author(s) and the published article's title, journal citation, and DOI. Users should also indicate if changes were made and avoid any implication that the author or Optica Publishing Group endorses the use.

**23 March 2023**

<https://hdl.handle.net/2440/131087>



# Preferential coupling of diamond NV centres in step-index fibres

SHUO LI,<sup>1,8</sup>  DONGBI BAI,<sup>2,9</sup>  MARCO CAPELLI,<sup>2</sup>  QIANG SUN,<sup>1</sup>   
SHAHRAAM AFSHAR V.,<sup>3</sup>  DAVID A. SIMPSON,<sup>4</sup>  SCOTT FOSTER,<sup>5</sup>  
HEIKE EBENDORFF-HEIDEPRIEM,<sup>6,7</sup>  BRANT C. GIBSON,<sup>1</sup>  AND  
ANDREW D. GREENTREE<sup>1,10</sup> 

<sup>1</sup>ARC Centre of Excellence for Nanoscale BioPhotonics, RMIT University, Melbourne, VIC 3001, Australia

<sup>2</sup>School of Science, RMIT University, Melbourne, VIC 3001, Australia

<sup>3</sup>UniSA STEM, University of South Australia, Adelaide, SA 5095, Australia

<sup>4</sup>School of Physics, The University of Melbourne, Melbourne, VIC 3010, Australia

<sup>5</sup>Defence Science and Technology Group, Edinburgh, SA 5111, Australia

<sup>6</sup>Institute for Photonics and Advanced Sensing, School of Physical Sciences, The University of Adelaide, Adelaide, SA 5005, Australia

<sup>7</sup>ARC Centre of Excellence for Nanoscale BioPhotonics, The University of Adelaide, Adelaide, SA 5005, Australia

<sup>8</sup>shuo.li3@rmit.edu.au

<sup>9</sup>baidongbi@gmail.com

<sup>10</sup>andrew.greentree@rmit.edu.au

**Abstract:** Diamonds containing the negatively charged nitrogen-vacancy centre are a promising system for room-temperature magnetometry. The combination of nano- and micro-diamond particles with optical fibres provides an option for deploying nitrogen-vacancy magnetometers in harsh and challenging environments. Here we numerically explore the coupling efficiency from nitrogen-vacancy centres within a diamond doped at the core/clad interface across a range of commercially available fibre types so as to inform the design process for a diamond in fibre magnetometers. We determine coupling efficiencies from nitrogen-vacancy centres to the guided modes of a step-index fibre and predict the optically detected magnetic resonance (ODMR) generated by an ensemble of four nitrogen-vacancy centres in this hybrid fibre system. Our results show that the coupling efficiency is enhanced with a high refractive index difference between the fibre core and cladding and depends on the radial position of the nitrogen-vacancy centres in the fibre core. Our ODMR simulations show that due to the preferential coupling of the nitrogen-vacancy emission to the fibre guided modes, certain magnetometry features such as ODMR contrast can be enhanced and lead to improved sensitivity in such diamond-fibre systems, relative to conventional diamond only ensemble geometries.

© 2021 Optical Society of America under the terms of the [OSA Open Access Publishing Agreement](https://doi.org/10.1364/OE.417825)

## 1. Introduction

The negatively-charged nitrogen-vacancy (NV) color centre in diamond has created entirely new opportunities for ultra-sensitive nanoscale magnetometry [1]. The key advantage of NV:diamond include nanoscale operating environment, biocompatibility and optical readout with high photostability. Collecting emission from either individual NV centres, or NV ensembles remains a critical issue limiting performance, and this often restricts NV magnetometry to laboratory-based environments, especially those where the biocompatibility of diamond can be used to greatest effect [1–3].

Motivated by a desire to apply NV sensor technology beyond the laboratory, there has been considerable effort in exploring the combination of NV centres with optical fibres. Early work considered attaching [4–6] or growing NV centres [7] to fibre end facet. More scalable approaches

include dip coating onto tapered fibre regions [8], or the use of in-fibre microfluidics to position diamond microparticles within the fibre core [2]. An alternative approach is to create hybrid diamond glass structures. Previous studies involved the embedding of diamond nanoparticles in soft tellurite glass [9,10]. This approach was successful in incorporating NV into optical fibre structures, but suffered from the problem that tellurite is a non-standard glass with poor mechanical properties. More recently diamond microparticles have been incorporated at the interface between the inner and outer regions of a robust lead silicate fibre by coating a cane with micro-diamond particles, then inserting this into a tube and drawing down into hybrid diamond fibre [11]. Similar technology could be applied to step-index fibre fabrication with the diamond particles at the core/clad interface.

Here we show detailed modelling that combines the coupling efficiencies expected for interface-doped NV nanoparticles as a function of core/clad properties with predictions of geometry-dependent ODMR contrast. Such modelling is necessary to optimise sensing in fibre-based architectures. Our modelling shows strong variation in the coupling efficiency as a function of core diameter, core/clad refractive index difference, position of the NV emitter relative to the interface, and NV crystallographic orientation. We find the preferential coupling from particular NV orientations into the guided modes of the fibres, with the relative couplings varying with the fibre parameters. When applied to NV magnetometry, we find that the preferential coupling changes the optically detected magnetic resonance (ODMR) contrast and limit of detection relative to what is expected for isotropic media, and this has implications for the use of NV:fibre magnetometers.

This paper is organised as follows: we begin by explaining the fibre systems we are considering, and the fundamental modelling methodology. We next explore the effects of core diameter and core/clad refractive index difference on the coupling efficiencies for the components of the NV orientations across our fibre types. Next, we consider the coupling with regards to relative position of the NV emitter to the core/clad interface. Finally we combine our modelling of the coupling efficiencies with predictions of ODMR signal expected through the guided modes of particular NV:fibre geometries, and analyze the ODMR limit of detection in the hybrid fibre.

## 2. Method

In this study we assume the nanodiamond particle size is infinitely small for simplicity and assume an ideal NV emitter existing in the hybrid fibre system. Strictly speaking, an NV centre consists of two linear dipoles in the plane perpendicular to the NV axis [12–14]. However, these two dipoles are incoherent with each other and any resultant fluorescence can be described as a superposition of the three dipole orientations in Fig. 1(b) [15]. Therefore, we treat the NV centre as an electric dipole, with the dipole moment orientation parallel to the nitrogen-vacancy axis. The fibre system is a typical step-index fibre with high-index glass as the core material and low-index glass as the cladding. In this study, we have ignored the role of the diamond refractive index in scattering. This approximation is effectively equivalent to considering the limit of an infinitesimally small nanoparticle. This allows us to combine two analytical models: the coupling of the NV centre emission into guided modes of a fibre and the ODMR spectrum into a model that describes qualitatively the performance of NV-fibre system for magnetometry. As the nanodiamond size becomes non-negligible (from around 100 nm to 1  $\mu\text{m}$ ), the effect of the refractive index mismatch will become larger, which will require more sophisticated numerical treatments than are used here [15].

### 2.1. Modelling the dipole-fibre coupling

We start the study with the effect of the core size on coupling, concentrating on the range 0-10  $\mu\text{m}$ , which is the standard fibre size in step-index fibre fabrication. We select three types of commercial available lead-silicate glass, LLF1 glass ( $n = 1.54$ ), F2 glass ( $n = 1.62$ ), SF57 glass

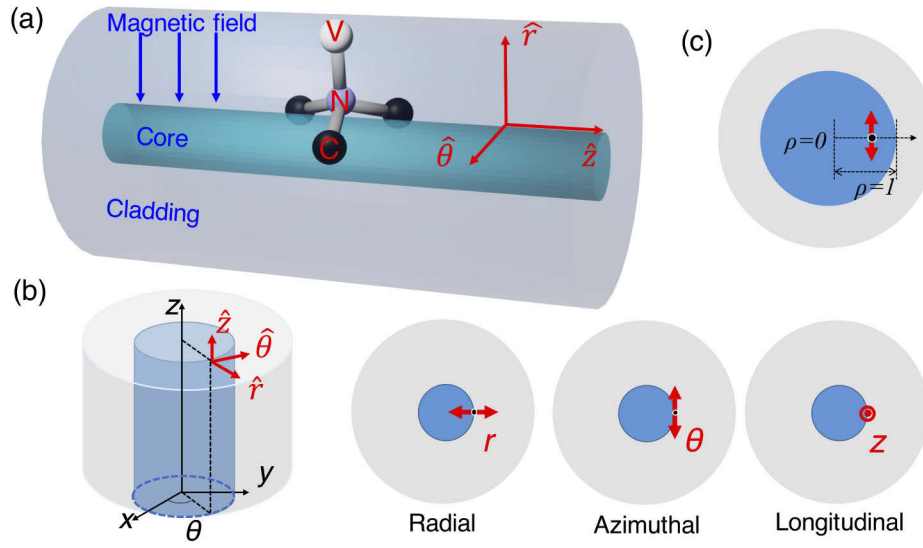


**Fig. 1.** (a) The schematic of a diamond NV centre in a step-index fibre. The blue and grey cylinders show the step-index fibre structure, and the NV centre is located at the core/clad interface. Blue arrows indicate the external magnetic field applied to the system. (b) Cylindrical coordinates in the fibre system. Cross sections of the fibre showing radial  $r$ -oriented, azimuthal  $\theta$ -oriented, and longitudinal  $z$ -oriented dipoles. The three orthogonal  $r$ -,  $\theta$ -,  $z$ -orientations in our simulation act as the superpositions of the four orientations of colour centres in a single diamond particle. (c) The schematic of changing the dipole radial position. The fibre centre and the core/clad interface are marked with the normalized radial position  $\rho = 0$  and  $\rho = 1$ , respectively.

( $n = 1.83$ ) as the fibre materials, which differ substantially in their refractive indices while having similar softening temperatures. This promises fabrication of core/clad fibers with a wide range of index contrasts of 0.08 for F2/LLF1, 0.21 for SF57/F2, and 0.29 for SF57/LLF1 for verification of the modeling in the future. Besides its high transparency and robustness, the relatively low softening temperature ( $<700$  °C) of lead-silicate glass is desirable to avoid damage to the NV either through diamond combustion, which occurs at 700 °C, or through annealing of NV centres at temperatures greater than 1000 °C [16]. During the interface doping process the highest temperature diamond is exposed to is the fibre drawing temperature, and the low softening temperature of these glasses make sure that the drawing is done at  $<700$  °C, which is below the onset of NV centre annealing.

We use a similar calculation procedure in our previous studies [17,18] with in-house MATLAB code (available upon request) to build the model. To model the dipole-fibre system, a dipole is located at the core/clad interface of a step-index fibre. The dipole moment is  $\mathbf{p}_0$  and position  $\mathbf{r}_0 = [r, \theta, z]$  oscillating with a frequency  $\omega$ . The fibre is modelled as a cylinder core with refractive index  $n_{co}$  surrounded by an infinite cladding with refractive index  $n_{cl}$ . The total guided electric field of the dipole-fibre system can be written as the sum of a series of discrete modes [17]:

$$\mathbf{E} = \sum_j a_j(z) \mathbf{e}_j e^{-i\beta_j z} + a_{-j}(z) \mathbf{e}_{-j} e^{i\beta_j z} \quad (1)$$

where  $\beta$  is the mode propagation constant,  $\mathbf{e}$  is the mode electric field expression, and  $a$  is the mode coefficient, for the  $j$ th mode of the fibre ( $kn_{cl} < \beta_j < kn_{co}$ , with  $-j$  denoting a backward propagating mode).

We use the reciprocity theorem to solve  $a_j$  [17,19]. The total dipole emission power coupled into the forward guided modes is calculated by summing the power  $P_j$  captured by each mode

$$P_{\text{total}} = \sum_j P_j, j = 1, 2, 3 \dots \quad (2a)$$

$$|a_j|^2 = \frac{\omega^2}{16N_j^2} |\mathbf{e}_j^*(\mathbf{r}_0) \cdot \mathbf{P}(\mathbf{r}_0)|^2 \quad (2b)$$

where  $P_j = |a_j|^2 N_j$ ,  $a_j$  is the mode coupling coefficient and  $N_j$  is a normalisation term. We define the coupling efficiency or coupling fraction of a forward guided mode as  $P_j/P_{\text{air}}$ , in which  $P_{\text{air}} = \mu_0 P_0 \omega^4 / 12\pi c$  is the total emitted power by the dipole in air. Note that this definition indicates the amount of power coupled to a mode of a step index fibre relative to the total power radiated in an unstructured isotropic material, the air. In the fibre core, the power captured by the forward and backward guided modes is the same, so the power measured in one fibre port is the same as the other port [20].

Fig. 1(a) illustrates the NV orientation with respect to the core/clad fibre geometry. Three orthogonal directions defined by the fibre geometry in Fig. 1(b), radial  $r$ -oriented, azimuthal  $\theta$ -oriented, and longitudinal  $z$ -oriented are considered as their coupling to the fibre depends on orientation. The dipole emission wavelength is set at 700 nm, which is close to the maximum of the NV centre spectral emission [21].

## 2.2. Modelling the ODMR signal

The dipole-fibre system described in the previous section impacts the ODMR signal of an ensemble of NV centres. Because of the preferential coupling, the ODMR signal from the NV-fibre system would be different from the diamond in a homogeneous environment. The diamond:fibre system we study for modelling the ODMR sensing is described in Fig. 1(a). We consider an ensemble of NVs at the core/clad interface of the F2/LLF1 fibre with a 1  $\mu\text{m}$  core. To illustrate the effect of the fibre geometry on the ODMR signal we consider one particular configuration, namely that with one NV orientation along the  $r$ -axis, a second NV on the  $r\theta$ -plane, and all others fixed by the  $sp^3$  structure of the diamond lattice, as shown in Fig. 6(a). The directions of the NV axes are converted to the cylindrical system of  $r, \theta, z$  by applying appropriate transformations from the Cartesian coordinate.

The typical ODMR spectrum is characterised by multiple Lorentzian dips subtracted from a constant emission intensity, representing the emission of the unperturbed off-resonant NV centre. The frequency at which the dips appear depends on the strength of the magnetic field applied to the NV centre and how the magnetic field vector projects onto the NV axis. We can predict the resonant frequencies by solving the ground state Hamiltonian of the NV centre reported in Eq. (2):[22]

$$\mathcal{H}_{\text{gs}} = D_g S_z^2 + \frac{g_{\text{NV}} \mu_B}{h} \mathbf{B} \cdot \mathbf{S} \quad (3)$$

where  $D_g = 2.87$  GHz is the NV ground state zero field splitting,  $\mu_B$  is the Bohr magneton,  $g_{\text{NV}} = 2.0023$  is the g-factor of the NV centre,  $h$  is Planck's constant, and  $\mathbf{B}$  and  $\mathbf{S}$  are the external magnetic field and spin vectors, respectively. The magnetic field component aligned to the symmetry axis of the NV centre contributes to the splitting of the  $|\pm 1\rangle$  states by the Zeeman effect, generating two ODMR dips for each NV centre orientation.

By diagonalizing and solving the eigenvalue of the Hamiltonian matrix in Eq. (3) we can get the eigen-energies of the NV centre states and then calculate the position of the resonant frequencies. We model the ODMR spectrum generated by one NV centre as two Lorentzian curves with fixed full-width half-maximum (FWHM). Here we assume the coupling has little effect on the FWHM of the ODMR signal. We choose a constant FWHM of 5 MHz, based on

common experimental parameters for NV centre ensembles at room temperature [1,23,24]. Once we generated the ODMR signal of a single NV centre, we map its dipole moment to the fibre system and calculate the dipole emission using the coupling model described above. The dipole emission of each orientation acts as the off-resonant emission intensity for the ODMR signal of the corresponding dipole.

In a single diamond crystal, there are four possible orientations for the NV centres within the diamond crystallographic structure. We assume that for ensemble sensing applications, each diamond particle embedded within a fibre has a significant number of NV centres, such that they are approximately equally distributed among all four possible orientations. The exact total number of NV centres in a diamond particle depends on the diamond fabrication parameters and post-fabrication processing. However, all NV centres with the same orientation have the same emission dipole and ODMR signature, with their exact number only contributing as a constant multiplicative factor. The multiplicative factor does not impact our simulation since the ODMR signal is normalized by the off-resonant intensity. Therefore, with the assumption of evenly distributed orientations, we simulated the total ODMR signal as the sum of the 4 independent dipoles corresponding to each possible NV orientation.

### 3. Results

#### 3.1. $r$ -, $\theta$ -, $z$ -orientation NV coupling in three fibre types

Following our recent cane-in-tube fabrication technique for diamond hybrid fibres [6], we first study the power captured by the fibre when the NV dipole is located at the core/clad interface of the fibre. For the three fibre types with index contrasts of 0.08 for F2/LLF1, 0.21 for SF57/F2, and 0.29 for SF57/LLF1, we calculate the dipole power captured by the guided modes in the fibre core  $P_{\text{guided}}$ , as a function of core diameter. Fig. 2 shows the power coupling to fibre guided modes for a range of fibre core sizes 0-10  $\mu\text{m}$ .

To show the effect of the fibre core/clad structure on coupling efficiency, the captured power of fibre guided modes is normalised with the dipole emitting power in air  $P_{\text{guided}}/P_{\text{air}}$ . For all three fibre types, the coupled power is typically greater for the radially  $r$ - and azimuthally  $\theta$ - oriented dipole components, while the coupling for the longitudinally  $z$ - oriented dipole component is approximately one order of magnitude lower than the other two orientations. Comparing the results of the three fibre-types, we find that dipole in SF57/LLF1 fibre, which has the highest refractive index contrast, shows the strongest coupling for each orientation. For  $r$ -oriented dipole, the fibre-dipole power capture is increased by a factor of 4 from low index difference fibre, F2/LLF1 fibre (average coupling fraction 3% for blue curve in Fig. 2(a)), to high index difference fibre, SF57/LLF1 fibre (average coupling fraction 12% for blue curve in Fig. 2(c)).

Different coupling features can be observed from the curves with regard to small and large core sizes. Because the emission rate can change dramatically for an emitter near an interface [18], for the small core diameter clear oscillation patterns are revealed from the the 0-3  $\mu\text{m}$  region (left of the dashed lines) in Fig. 2(a)-(c); the oscillation peak separation increases with the decrease of core/clad index difference. For the relatively large fibre core sizes above 3  $\mu\text{m}$  region (right of the dashed lines in Fig. 2(a)-(c)), coupling does not change significantly when the core size increases. Fibres with large core sizes intrinsically support more higher-order modes, but the power carried by each higher-order mode is small so the total captured power stays relatively steady. Additionally, the coupling differences among  $r$ ,  $\theta$ ,  $z$  increase with the increase of index difference. Black dashed lines at 3  $\mu\text{m}$  indicate the transition from the oscillatory region to relatively stable region.

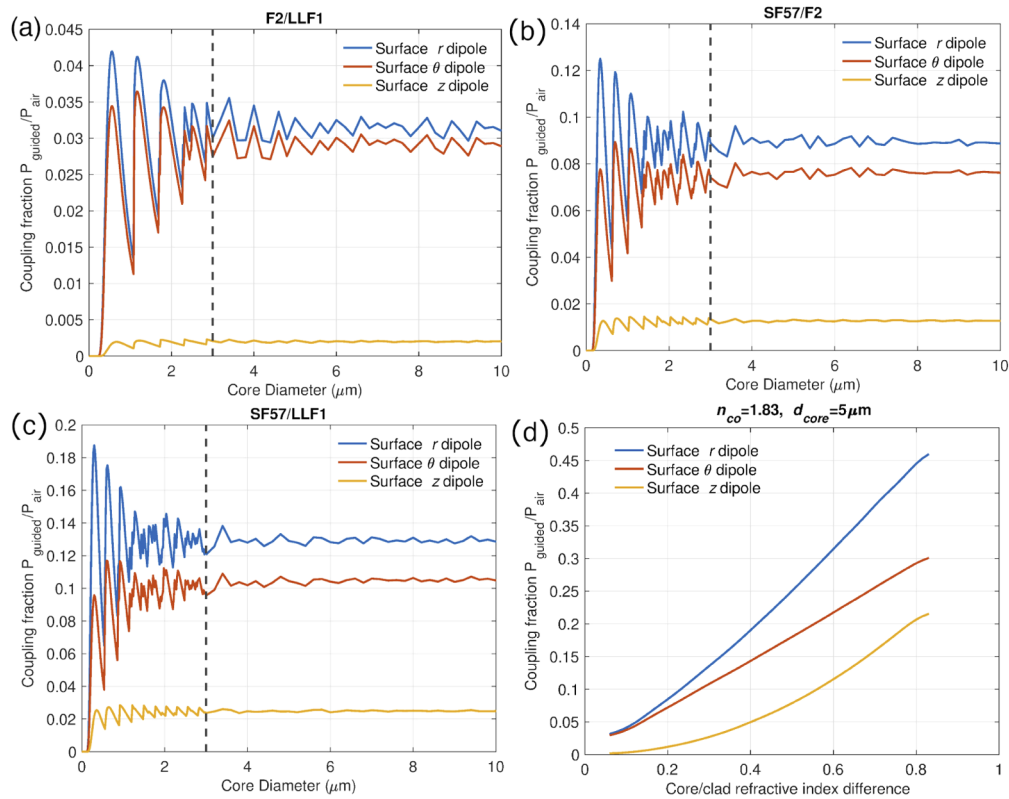


**Fig. 2.** Normalized dipole power coupling fractions  $P_{\text{guided}}/P_{\text{air}}$  into guided modes of (a) F2/LLF1 fibre, (b) SF57/F2 fibre, (c) SF57/LLF1 fibre versus fibre core diameter. Blue, red, yellow curves represent  $r$ -,  $\theta$ -,  $z$ -oriented dipole, respectively. Black dashed lines at  $3\mu\text{m}$  indicate the transition from the oscillatory region to relatively stable region. (d) Power coupled to guided mode vs. core/clad index difference, with fixed core diameter of  $5\mu\text{m}$  and refractive index of 1.83 for SF57 glass. The coupling efficiency increases with the increasing core/clad refractive index difference, and the differences between the three oriented dipole coupling become more significant.

### 3.2. Coupling vs. fibre core/clad index difference

Based on the results previously described, we investigate the power coupling against the refractive index difference of the fibre core and cladding. The fibre is fixed at a core size of  $5\mu\text{m}$  and the core refractive index is kept at 1.83, the highest refractive index of the three lead-silicate glass. We run the calculation by changing the cladding refractive index and observing the change in the coupling efficiency. As Fig. 2(d) shows, as the refractive index difference increases, the coupled power increases, and the difference between  $r$ -,  $\theta$  and  $z$ -oriented dipole coupling becomes significant. Our results indicate that high index difference of fibre core/clad is generally favourable for achieving high coupling efficiency from the dipole to the fibre, which is in keeping with previous results on air-clad fibres [17].

### 3.3. Coupling vs. NV position along radial-direction

Besides the mentioned interface dipole coupling, to further understand the influence of NV position on fibre power capture, we also investigate the coupling with different dipole radial positions using the F2/LLF1 fibre ( $n_{\text{co}} = 1.62, n_{\text{cl}} = 1.54$ ) as an example. We varied the location

of the dipole radially by moving it from the fibre core centre to the fibre cladding area, as shown in Fig. 1(c). The normalised dipole position  $\rho$  is defined as the dipole radial position normalized by the fibre core radius,  $\rho = r_{\text{dipole}}/r_{\text{core}}$ . The core centre is at the origin, and  $\rho < 1$  indicates that the NV centre is inside the fibre core. Fig. 3 presents the coupling from the  $r$ -,  $\theta$ -,  $z$ -oriented dipole, respectively, with regards to dipole radial position and core diameter. As expected, radial and azimuthal orientated dipoles show stronger coupling than the longitudinal orientated dipole. The bright yellow bands, which are highlighted with black dash lines in Fig. 3(a)-(c), indicate the maximum coupling under different fibre core sizes. With increasing core size, the optimal dipole position approaches the interface from the core side. When the core size is  $< 2 \mu\text{m}$ , the maximum coupling occurs when the dipole is located in the central region of the fibre core (with approx.  $\rho < 0.8$ ). When the core size is  $2 \mu\text{m}$ , the maximum coupling occurs when the dipole is positioned near the core/clad interface (at a location slightly smaller than the core radius, i.e. at  $\rho = 0.8 - 0.9$  for the  $r$ - and  $\theta$ -oriented dipole), but not exactly on the interface.

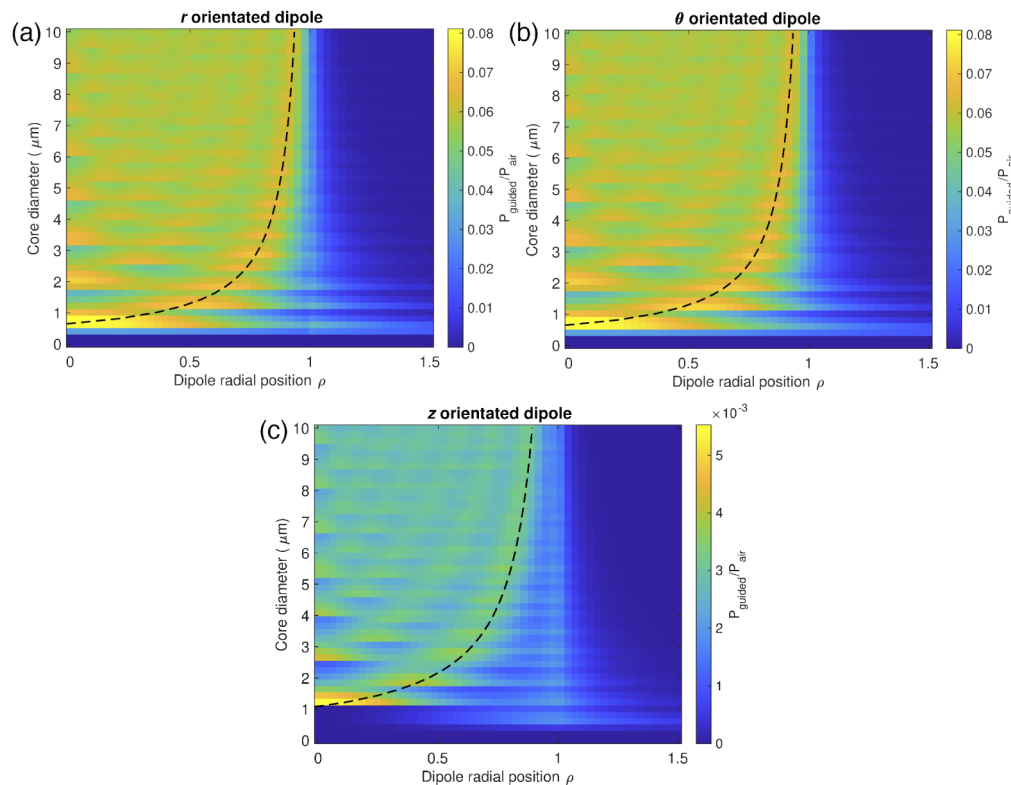


**Fig. 3.** Normalized power captured by fibre guided modes  $P_{\text{guided}}/P_{\text{air}}$  versus dipole radial positions and also a range of core diameters for  $r$ - (a),  $\theta$ - (b) and  $z$ - (c) orientated dipoles, with x-axis as dipole position, y-axis as fibre core size. The fibre configuration is F2/LLF1 ( $n_{\text{co}}/n_{\text{cl}}$ : 1.62/1.54). The black dash lines on each plot indicate the region of maximum coupling to the fibre guided modes.

It is interesting to find that for small core sizes, about  $< 2 \mu\text{m}$ , the coupling power decreases monotonically with the dipole position moving away from the core centre, and the maximum coupling usually happens when the dipole locates in the central region. However, the situation is different for core sizes  $> 2 \mu\text{m}$ . For large core size ( $> 2 \mu\text{m}$ ) the coupling power stays relatively steady as long as the dipole is inside the core region, generating the maximum coupling when the dipole is near the interface and the coupling starts to decrease only when the dipole reaches the



core/clad interface. Furthermore, the coupling drops off exponentially when the dipole is outside of the core region corresponding to the evanescent wing.

To analyze the optimal dipole position, Fig. 4 presents the power into guided modes at different dipole locations. Take the  $r$ -oriented dipole as an example, using a core size of  $2\ \mu\text{m}$ , the dipole positioned at the core centre achieved the highest coupling, while with a core size of  $3\ \mu\text{m}$  the dipole with highest coupling is located near the interface. The curves show the coupling power for each individual guided mode.

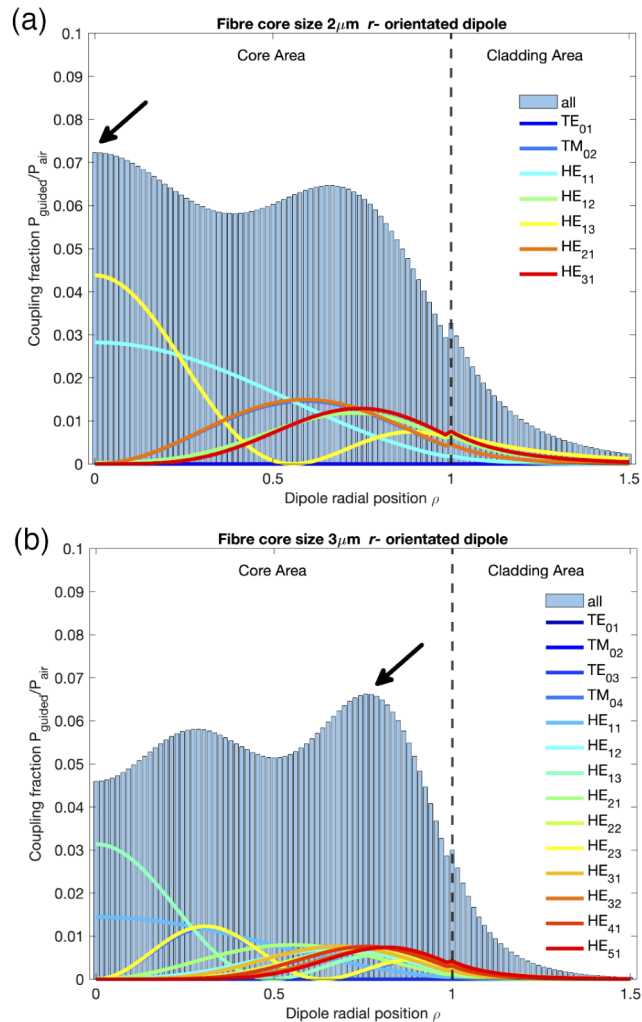


**Fig. 4.** Coupling fraction of  $P_{\text{guided}}/P_{\text{air}}$  for all modes supported within a fibre core size of (a)  $2\ \mu\text{m}$  and (b)  $3\ \mu\text{m}$  for an  $r$ -oriented dipole. Modes decomposition for (a)  $2\ \mu\text{m}$  and (b)  $3\ \mu\text{m}$  diameter cores for comparison (F2/LLF1,  $n_{\text{co}}/n_{\text{cl}}$ : 1.62/1.54). The dashed lines show the core/clad interface position separating the core and cladding areas, and the optimal dipole coupling positions are indicated by arrows, in fibre core centre of (a) and near the interface of (b). The total guided mode power (blue bars) is decomposed into individual mode power shown by the colored solid lines.

The observed results relate to the density of states in a fibre core. In the fibre core the low-order modes have energy in the central area, e.g. the fundamental mode or the 2<sup>nd</sup> order modes;

whereas higher-order modes usually have small  $\mathbf{E}$  field strength in the central area and energy mostly concentrate in the edge area of the core. Only limited guided modes can be supported by small size fibre core, so when the core size is small the dipole power can only realize field overlap with few low order modes to easily couple into. When the dipole locates at the edge area of the fibre core, the dipole field is more likely to overlap with higher-order modes. Though the fundamental mode and 2<sup>nd</sup> order modes have relative high energy compare with individual higher-order mode, the total power of all the higher-order modes can still reach a higher value, as the black arrows indicating in Fig. 4. For large core size like 10  $\mu\text{m}$ , the total number of guided modes excited by the interface dipole could be more than 100 at 700 nm. But usually higher-order modes occupy a small fraction of the total fibre captured power from a dipole, so increasing the core size would not make the maximum coupling change significantly.

### 3.4. ODMR simulation for a ensemble of NVs in a fibre

Figure 5 compares the ODMR spectra from an NV ensemble at the fibre core/clad interface (blue) with the ODMR spectra from the same NV ensemble in air without fibre (red). In this simulation the coupling power only changes the ODMR off-resonant intensity, and the ODMR pattern is determined by the relative angle between the external magnetic field  $\mathbf{B}$  and the NV ensemble orientation. Several magnetic field directions are studied here, with direction along  $r$ ,  $\theta$ ,  $z$  respectively (Fig. 5(a)-(c)) and the one with all three components [3, 3, 2] (Fig. 5(d)). In Fig. 5(d) we set the external magnetic field such that its vector is not perpendicular to any of the possible NV orientations. The ODMR signal as a function of magnetic field shows the Zeeman effect of the unpaired electronic spins of the NV centre. As shown in Eq. (3), each NV centre has a spin 1 ground state manifold with zero field splitting of approximately 2.87 GHz, and hence contributes two dips to the ODMR spectrum, for the  $|0\rangle$  to  $|+1\rangle$  and  $|0\rangle$  to  $|-1\rangle$  transitions. Each distinct NV orientation in a single nanodiamond particle generates 2 resonant frequencies, for a total of eight distinguishable dips when modelling the full ensemble of NV centres [1].

For a ensemble of NV centres, the ODMR contrast would change because of different coupling in  $r$ ,  $\theta$ ,  $z$  directions, compare with ensemble NVs in single crystal diamond. This contrast with the largest ODMR dip is calculated. At certain magnetic field direction e.g [0, 0, 1] for this NV ensemble orientation, the fibre modifies the contrast to 11%, compare with 8% in no fibre scenario. The fibre couples most of the dipole power into  $r$  and  $\theta$  directions and suppresses the  $z$ - direction, therefore when the largest dip is generated mainly by  $r$  and  $\theta$  components from ensemble NVs under certain  $\mathbf{B}$  field directions, the contrast would increase, enhancing certain features relative to others.

We also explore ODMRs from different NV ensembles. ODMRs in Fig. 6(c) are generated by two differently orientated ensembles of NV centres core/clad-doped in an F2/LLF1 fibre under the  $\mathbf{B}$  field direction  $(r, \theta, z)$  [3,4,2]. Based on the relative angles between the fixed magnetic field vector and the dipoles of each ensemble, we can see up to eight dips in the spectra, indicating all four NV orientations considered in the simulation. The ensemble of NVs in Fig. 6(a) has the same orientation as Fig. 1(a), which is defined in detail in Section 2.2, and Fig. 6(b) orientation is obtained by rotating the full tetrahedron in Fig. 6(a) around the  $\theta$ -axis by an azimuthal angle  $\arccos \frac{1}{\sqrt{3}}$  and then around the  $r$ -axis by a polar angle  $\pi/4$ . The contrast generated by Fig. 6(a) is high because the ensemble orientation is more aligned with the external magnetic field.

### 3.5. ODMR contrast analysis for three fibre types

Based on the different ratio of  $r$ ,  $\theta$ ,  $z$  coupling in the three lead-silicate fibres, we compare the ODMR contrasts from the three fibres systems. We calculate ratio of  $r$ ,  $\theta$ ,  $z$  coupling fraction in Fig. 2(a-c), and Table 1 presents the maximum ODMR contrasts for three fibres F2/LLF1, SF57/F2 and SF57/LLF1 with core size 1  $\mu\text{m}$ , with the magnetic field direction along the  $r$  axis and contrasts 5.026%, 4.96%, 5.008%. The ODMR contrast depends on the power ratio of the

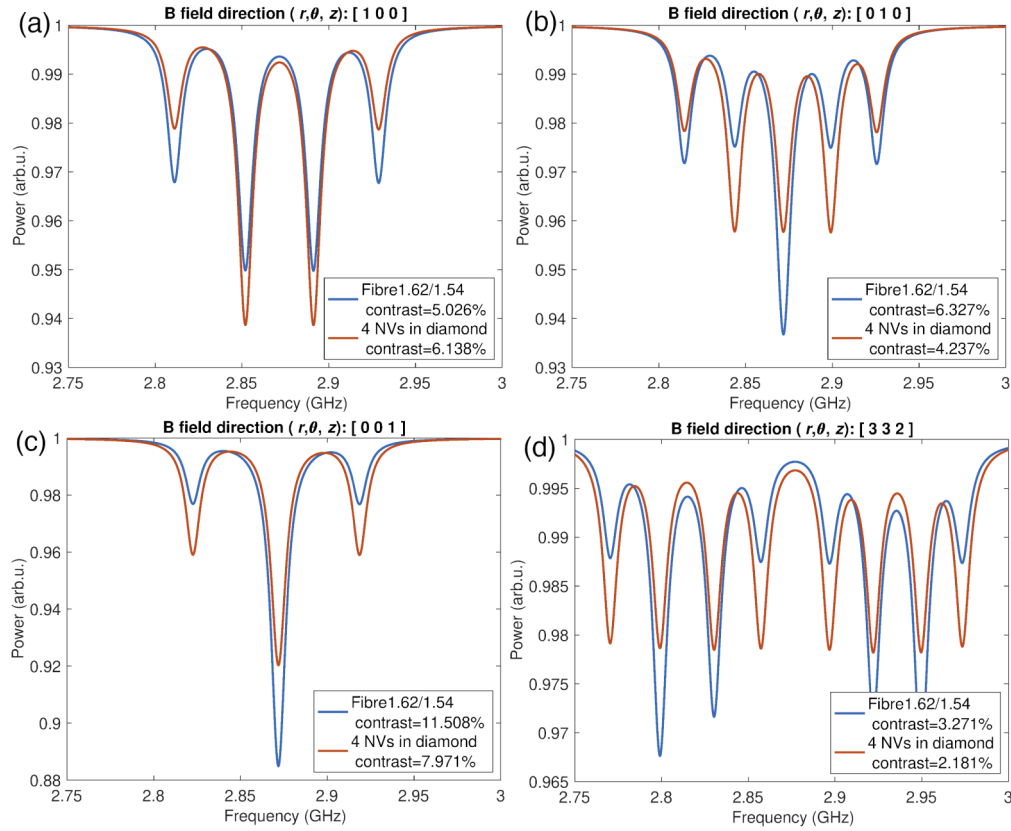


**Fig. 5.** Simulated ODMR signals generated by an ensemble of four NVs in a F2/LLF1 fibre under different magnetic fields. The  $\mathbf{B}$  direction is along (a)  $r$ , (b)  $\theta$ , (c)  $z$  axis, and (d) with all three components [3, 3, 2]. (a)-(c)  $\mathbf{B}$  strength 2.1 mT, (d)  $\mathbf{B}$  strength 4.2 mT to separate eight dips.

three orthogonal orientations  $r, \theta, z$ . The difference is subtle because of the similar coupling ratios among  $r, \theta, z$  in these three fibre types.

**Table 1.** The ratio of  $r, \theta, z$  coupling fraction and the ODMR contrast in three fibres.

Fibre type	$r$	$\theta$	$z$	ODMR contrast
F2/LLF1 (1.62/1.54)	0.5063	0.4623	0.0314	5.026%
SF57/LLF1 (1.83/1.54)	0.5068	0.3978	0.0953	4.96%
SF457/F2 (1.83/1.62)	0.5069	0.4214	0.0717	5.008%

### 3.6. ODMR limit of detection vs. core/clad index difference

Next we explore the effect of core/clad index difference on ODMR limit of detection under different magnetic field directions. Based on the ODMR sensitivity  $\eta$  determined in [9]

$$\eta = \frac{4h\delta}{3\sqrt{3}g_{\text{NV}}\mu_{\text{B}}C\sqrt{N}} \quad (4)$$

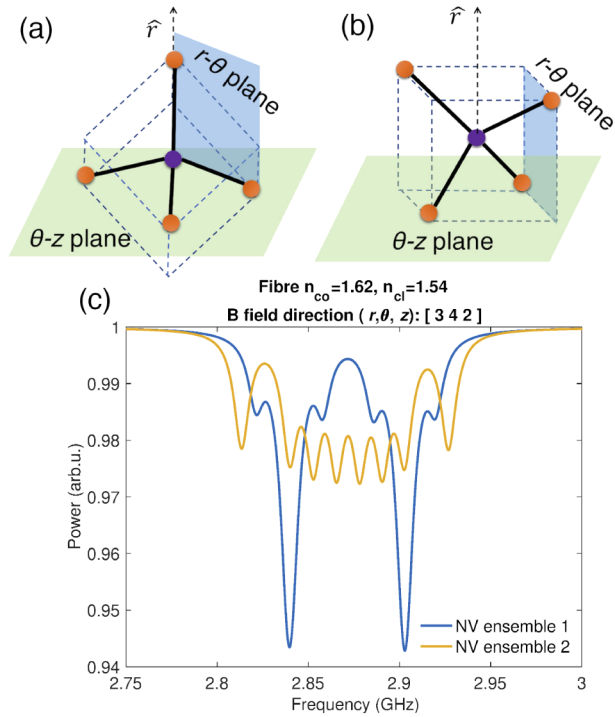


**Fig. 6.** (a)-(b) Coordinates in the fibre of two differently orientated ensembles of NV centres, respectively. (c) The simulated ODMR signals from the NV ensemble 1 in (a) (blue) and the NV ensemble 2 in (b) (yellow) core/clad-doped in a F2/LLF1 fibre under the  $\mathbf{B}$  field direction  $(r, \theta, z)$  [3,4,2] and strength 2.1 mT.

where  $\delta$  is the FWHM of the ODMR peak,  $C$  is the ODMR contrast,  $g_{NV}$  is the g-factor of the NV centre and  $\mu_B$  is the Bohr magneton.  $N$  is the number of photons per second detected at the output end of the fiber.

We use here the limit of detection which is defined as a relative value normalized to the ODMR sensitivity of the same diamond structure in air surrounding,  $\eta_{\text{relative}} = \eta_{\text{fibre}}/\eta_{\text{air}}$ , to highlight the effect of the fibre. The results are shown in Fig. 7 in log scale with the magnetic field directions corresponding to Fig. 5 sub-figures. When  $\eta_{\text{relative}} < 10^0$ , the diamond:fibre system shows limit of detection improvement comparing with the ensemble of four NVs in air. The results indicate that the limit of detection increases with the increased core/clad index difference. From Fig. 7(b)-(d) it can be seen that with large enough core/clad index difference, e.g. when fibre core is  $2\mu\text{m}$  with the core/clad index  $> 0.8$  at certain  $\mathbf{B}$  field direction [0,1,0] and [3,3,2], the value of  $\eta_{\text{relative}}$  can reach  $< 0.59$ . Since the ODMR sensitivity  $\eta$  in Eq. (4) is in the unit  $\text{T}/\sqrt{\text{Hz}}$  and its value showing the minimal magnetic field change in detection, the improvement of the limit of detection can be measured with  $1/\eta_{\text{relative}}$ . By this definition  $\eta_{\text{relative}}$  value  $< 0.59$  indicates that the preferential coupling of fibre structure could improve the limit of detection to 1.6 times higher than no-fibre scenario. The limit of detection changes less significantly with core size, considering the coupling efficiency stays relatively steady when core size is over  $3\mu\text{m}$ .

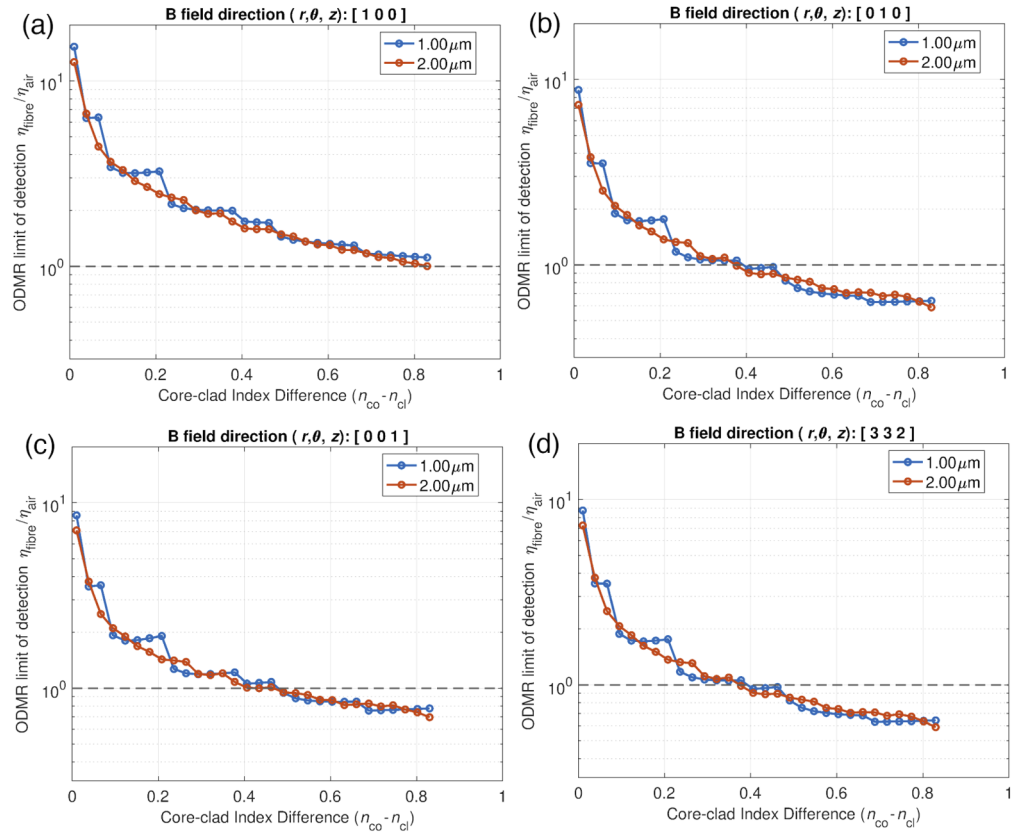


**Fig. 7.** ODMR limit of detection of an ensemble of four NVs in a step-index fibre vs. the fibre core/clad index configuration, under different magnetic fields. The  $\mathbf{B}$  direction is along (a)  $r$ , (b)  $\theta$ , (c)  $z$  axis, and (d) with all three components [3, 3, 2]. (a)-(c)  $\mathbf{B}$  strength 2.1 mT, (d)  $\mathbf{B}$  strength 4.2 mT to separate eight dips.

#### 4. Conclusion

In conclusion, we develop an emitter:waveguide model to study the coupling from dipole emissions into the guided modes of a step-index waveguide and apply this model for NV:diamond - fibre magnetometry. We find out the preferential coupling effect of the NV:diamond - fibre system and we investigate the coupling of different dipole orientations for (i) core/clad index contrast, (ii) core diameter, (iii) radial position of the NV emitters within the core, when radial position goes from the core centre to the core/clad interface. The study reveals that the coupling fraction of NV emission is enhanced with high refractive index difference between the fibre core and cladding, and we find out that the preferential coupling of particular NV dipole orientations increases the ODMR contrast at some configurations compared with ODMR in free space. Combining the coupling efficiencies with ODMR signals, the diamond doped step-index fibre system could lead to an improved magnetometry by enhancing the sensitivity compared with NV centres in isotropic materials. Our model for the first time connects the NV dipole-in-fibre coupling to the resulting ODMR sensing properties, and the results provide new perspectives in the design and fabrication of future NV-in-fibre protocols.

**Funding.** Defence Science and Technology Group under the Next Generation Technologies Fund; ARC Centre of Excellence for Nanoscale BioPhotonics (CE140100003); Australian Research Council (FT160100357); Asian Office of Aerospace Research and Development (FA2386-18-1-4056).

**Acknowledgments.** The authors thank Dr. M. R. Henderson for his modelling work done for tellurite glass fibre, which laid a good foundation for this study.

**Disclosures.** The authors declare no conflicts of interest.

## References

1. L. Rondin, J. P. Tetienne, T. Hingant, J. F. Roch, P. Maletinsky, and V. Jacques, "Magnetometry with nitrogen-vacancy defects in diamond," *Rep. Prog. Phys.* **77**(5), 056503 (2014).
2. S. Maayani, C. Foy, D. Englund, and Y. Fink, "Distributed quantum fiber magnetometry," *Laser Photonics Rev.* **13**(7), 1900075 (2019).
3. L. P. McGuinness, Y. Yan, A. Stacey, D. A. Simpson, L. T. Hall, D. Maclaurin, S. Praver, P. Mulvaney, J. Wrachtrup, F. Caruso, R. E. Scholten, and L. C. L. Hollenberg, "Quantum measurement and orientation tracking of fluorescent nanodiamonds inside living cells," *Nat. Nanotechnol.* **6**(6), 358–363 (2011).
4. R. Albrecht, A. Bommer, C. Pauly, F. Mücklich, A. W. Schell, P. Engel, T. Schröder, O. Benson, J. Reichel, and C. Becher, "Narrow-band single photon emission at room temperature based on a single nitrogen-vacancy center coupled to an all-fiber-cavity," *Appl. Phys. Lett.* **105**(7), 073113 (2014).
5. D. Duan, V. K. Kavatamane, S. R. Arumugam, G. Rahane, Y.-K. Tzeng, H.-C. Chang, H. Sumiya, S. Onoda, J. Isoya, and G. Balasubramanian, "Enhancing fluorescence excitation and collection from the nitrogen-vacancy center in diamond through a micro-concave mirror," *Appl. Phys. Lett.* **113**(4), 041107 (2018).
6. I. V. Fedotov, S. M. Blakley, E. E. Serebryannikov, P. Hemmer, M. O. Scully, and A. M. Zheltikov, "High-resolution magnetic field imaging with a nitrogen-vacancy diamond sensor integrated with a photonic-crystal fiber," *Opt. Lett.* **41**(3), 472–475 (2016).
7. J. R. Rabeau, S. T. Huntington, A. D. Greentree, and S. Praver, "Diamond chemical-vapor deposition on optical fibers for fluorescence waveguiding," *Appl. Phys. Lett.* **86**(13), 134104 (2005).
8. T. Schröder, M. Fujiwara, T. Noda, H.-Q. Zhao, O. Benson, and S. Takeuchi, "A nanodiamond-tapered fiber system with high single-mode coupling efficiency," *Opt. Express* **20**(10), 10490–10497 (2012).
9. Y. Ruan, D. A. Simpson, J. Jeske, H. Ebendorff-Heidepriem, D. W. M. Lau, H. Ji, B. C. Johnson, T. Ohshima, S. Afshar V, L. Hollenberg, A. D. Greentree, T. M. Monro, and B. C. Gibson, "Magnetically sensitive nanodiamond-doped tellurite glass fibers," *Sci. Rep.* **8**(1), 1268 (2018).
10. M. R. Henderson, B. C. Gibson, H. Ebendorff-Heidepriem, K. Kuan, S. Afshar V, J. O. Orwa, I. Aharonovich, S. Tomljenovic-Hanic, A. D. Greentree, S. Praver, and T. M. Monro, "Diamond in tellurite glass: a new medium for quantum information," *Adv. Mater.* **23**(25), 2806–2810 (2011).
11. D. Bai, M. H. Huynh, D. A. Simpson, P. Reineck, S. A. Vahid, A. D. Greentree, S. Foster, H. Ebendorff-Heidepriem, and B. C. Gibson, "Fluorescent diamond microparticle doped glass fiber for magnetic field sensing," *APL Mater.* **8**(8), 081102 (2020).
12. T. P. M. Alegre, C. Santori, G. Medeiros-Ribeiro, and R. G. Beausoleil, "Polarization-selective excitation of nitrogen vacancy centers in diamond," *Phys. Rev. B* **76**(16), 165205 (2007).
13. A. Batalov, V. Jacques, F. Kaiser, P. Siyushev, P. Neumann, L. J. Rogers, R. L. McMurtrie, N. B. Manson, F. Jelezko, and J. Wrachtrup, "Low temperature studies of the excited-state structure of negatively charged nitrogen-vacancy color centers in diamond," *Phys. Rev. Lett.* **102**(19), 195506 (2009).
14. T. Schröder, A. W. Schell, G. Kewes, T. Aichele, and O. Benson, "Fiber-integrated diamond-based single photon source," *Nano Lett.* **11**(1), 198–202 (2011).
15. M. Almokhtar, M. Fujiwara, H. Takashima, and S. Takeuchi, "Numerical simulations of nanodiamond nitrogen-vacancy centers coupled with tapered optical fibers as hybrid quantum nanophotonic devices," *Opt. Express* **22**(17), 20045–20059 (2014).
16. J. O. Orwa, C. Santori, K. M. C. Fu, B. Gibson, D. Simpson, I. Aharonovich, A. Stacey, A. Cimmino, P. Balog, M. Markham, D. Twitchen, A. D. Greentree, R. G. Beausoleil, and S. Praver, "Engineering of nitrogen-vacancy color centers in high purity diamond by ion implantation and annealing," *J. Appl. Phys.* **109**(8), 083530 (2011).
17. M. R. Henderson, S. Afshar V, A. D. Greentree, and T. M. Monro, "Dipole emitters in fiber: interface effects, collection efficiency and optimization," *Opt. Express* **19**(17), 16182–16194 (2011).
18. M. R. Henderson, "Nanodiamond in optical fibre," Thesis, The University of Adelaide (2013).
19. A. W. Snyder and J. Love, *Optical waveguide theory* (Springer Science & Business Media, 2012).
20. M. Fujiwara, K. Toubaru, T. Noda, H.-Q. Zhao, and S. Takeuchi, "Highly efficient coupling of photons from nanoemitters into single-mode optical fibers," *Nano Lett.* **11**(10), 4362–4365 (2011).
21. L. Rondin, G. Dantelle, A. Slablab, F. Grosshans, F. Treussart, P. Bergonzo, S. Perruchas, T. Gacoin, M. Chaigneau, H. C. Chang, V. Jacques, and J. F. Roch, "Surface-induced charge state conversion of nitrogen-vacancy defects in nanodiamonds," *Phys. Rev. B* **82**(11), 115449 (2010).
22. M. W. Doherty, N. B. Manson, P. Delaney, F. Jelezko, J. Wrachtrup, and L. C. Hollenberg, "The nitrogen-vacancy colour centre in diamond," *Phys. Rep.* **528**(1), 1–45 (2013).
23. J. F. Barry, J. M. Schloss, E. Bauch, M. J. Turner, C. A. Hart, L. M. Pham, and R. L. Walsworth, "Sensitivity optimization for nv-diamond magnetometry," *Rev. Mod. Phys.* **92**(1), 015004 (2020).
24. A. Dréau, M. Lesik, L. Rondin, P. Spinicelli, O. Arcizet, J.-F. Roch, and V. Jacques, "Avoiding power broadening in optically detected magnetic resonance of single nv defects for enhanced dc magnetic field sensitivity," *Phys. Rev. B* **84**(19), 195204 (2011).